A Spatial FFT and FX Correlator for the BEST-2 Array

G. Foster[1], J. Hickish[1], D. Price[1], K. Zarb Adami[1]

[1] *Oxford University, Department of Physics*

31 March 2012

ABSTRACT

A new FX correlator and a spatial FFT imager has been developed using CASPER FPGA hardware for the BEST-2 array at the Radiotelescopi di Medicina in Italy. Both instruments use the same digitizing/channelizing front end. The spatial FFT imager takes advantage of BEST-2 as a regularly gridded array to perform a 2D spatial FFT using $O(n \log n)$ operations. The FX correlator has been used to solve complex gain calibrations which are applied in the spatial FFT during observation. During the initial deployment of the instruments several bright radio sources were observed over multiple epochs. An analysis of the spatial FFT imager baseline quality is performed and compared to that of the FX correlator. Our study shows the spatial FFT data to be comparable in quality to the FX correlator. Further methods can be implemented in the real time calibration and post integration calibration to improve the spatial FFT data quality.

1 INTRODUCTION

The Basic Element for SKA Training (BEST) 2 array is a subset of the Northern Cross cylindrical array, at the Radiotelescopi di Medicina in Italy. In this paper we describe a new digital backend designed for this array, implemented on CASPER (Parsons et al. 2006) designed FPGA-based hardware for fast correlation, direct imaging, beamforming and transient processing capabilities.

This digital backend consists of a 32 element digitizer, FX correlator, spatial FFT imager and beamformer implemented on ROACH FPGA boards. Of particular interest is the spatial FFT imager which can produce a complete set of unique baselines using $0(n \log n)$ operations by taking advantage of the regularly gridded antenna geometry. The FX correlator computes all possible baseline pairs which scales as $0(n^2)$. Along with producing correlation data the spatial FFT functions as a gridded beamformer which has been used for pulsar obersavtions. These instruments have been installed as prototypes for larger scale instruments currently in development. The correlator is being used to study the handling of large output data rates and the development of real time millisecond imaging using many antenna elements. The direct imaging system is being used to study the feasibility of such systems in arrays with regular geometric structure, as well as providing a platform for pulsar surveys and space-debris tracking capabilities with BEST-2. Since deployment, a number of sources with the correlator and imager have been successfully observed. Data has been reduced and calibrated using a combination of custom software and standard radio synthesis imaging packages.

In the first section of this paper we give an overview of the BEST-2 Array, followed by a description of the channelization, correlation and image-domain processing systems in Sections 2.1, 2.2 and 2.3, respectively. Results from preliminary observations of bright radio sources from these systems are presented in section 3.1 and a comparison of data quality between the two instruments is presented in section 4, with a discussion in section 5.

1.1 BEST-2 Array

The BEST-2 testbed at the Medicina Radio Observatory consists of 8 East-West oriented cylindrical concentrators, each with 64 dipole receivers critically sampling for focal line at 408MHz. These 64 dipoles are summed in groups of 16, resulting in 4 channels per cylinder, and a total of 32 effective receiving elements laid out on a *4-by-8* grid, fig. 1a.

BEST-2 was developed as a reliable, low cost frontend to be used in SKA development, with a core design requirement of simplicity in interfacing with different digital backends (Montebugnoli et al. 2009b). Extensive documentation of the

BEST-2 Array Specifications		
Cylinder & Element Properties		
Number of RX per Cylinder	4	
Cylinder Diameter	7.5	m
Cylinder Length	23.5	m
Element Diameter	7.5	m
Element Length	5.88	m
Element Collecting Area	44.1	m^2
Aperture Efficiency	0.71	
Element Effective Area	31.3	m^2
BEST-2 Array Properties		
Number of Cylinders	8	
Total Number of RX	32	
Total Collective Area	1411.2	m^2
Total Effective Area	1001.95	m^2
Sensitivity / Ant. gain	0.36	K/Jy
A_{eff}/T_{sys}	11.65	m^2/K
Antenna Temperature	35	K
Receiver Temperature	51	K
System Temperature	86	K
Longest Baseline		
E-W	17.04	m
N-S	70.00	m
Bandpass		
Central Frequency	408	MHz
Analog Bandwidth	16	MHz
Pointing Limits		
Declination	(0,+90)	deg
Right Ascension	Local Meridian	
Primary Beam		
Primary Beam Size	37.62	deg^2
Declination	5.7	deg
Right Ascension	6.6	deg
PSF		
PSF FWHM	0.9	deg^2
Declination	0.52	deg
Right ascension	1.73	deg

Table 1. The top level specifications of the BEST-2 Array, a subset of the collecting area of the Northern Cross, located in Medicina, Italy.

development of the BEST-2 analogue chain can be found in a number of papers (Perini 2009) (Perini et al. 2009). The top level specifications of the array are shown in table 1.

In 2008 the initial digital correlator backend of the array was based on iBOB and BEE2 FPGA boards from the Collaboration for Astronomy Signal Processing and Electronics Research (CASPER)(Montebugnoli et al. 2009a). An upgraded digital backend has been developed using the ROACH board, also developed by CASPER, which includes an FX correlator, spatial FFT imager and beamformer.
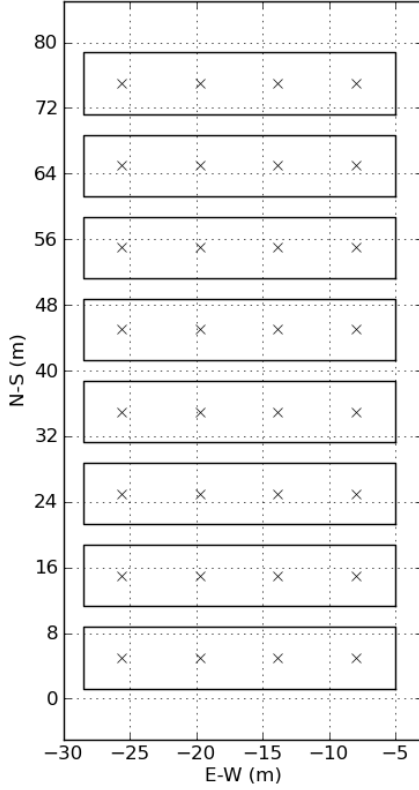
(a) The 32 effective receiving elements of BEST-2, indicated by crosses, lie on a regular 4x8 grid. Each receiver is the analogue sum of 16 dipoles, critically spaced at 408 MHz in the East-West direction.

(b) BEST-2 is a subset of eight cylinders in the north-south arm of the Croce del Nord.

Figure 1. BEST-2 antenna geometry.

2 INSTRUMENT DESIGN

An FX correlator and spatial FFT imager instrument have been built for BEST-2. The hybrid design of our digital instruments make it possible to use both the correlator and imager concurrently. Both instruments use the same digitization and channelization frontend. This allow a streamlined process of calibrating the spatial FFT imager, reduces the amount of hardware and allows for simultaneous observation with both instruments. The instrument has been implemented on ROACH boards which are a generic field programmable gate array (FPGA) board designed by CASPER for radio astronomy applications. A ROACH consist of a XILINX Virtex 5 SX95T FPGA with interfaces to DRAM and QDR memory, high speed CX-4 connectors and a generic Z-DOK interface for connecting ADCs and various daughter boards, fig 2. Additionally, the board has a PowerPC running BORPH, a variant of Debian Linux, which allows access to software registers and shared memory on the FPGA. Firmware is designed using MATLAB Simulink which is extended with XILINX DSP blocks and CASPER's open source DSP blocks[1]. Design specific DSP blocks and hardware interfaces have also created, design models and control software are available from our project repository[2]. Instrument design specifications are presented in table 2, further design detail is described in sections 2.1, 2.2 and 2.3.

---

[1] https://casper.berkeley.edu/
[2] https://github.com/griffinfoster/medicina
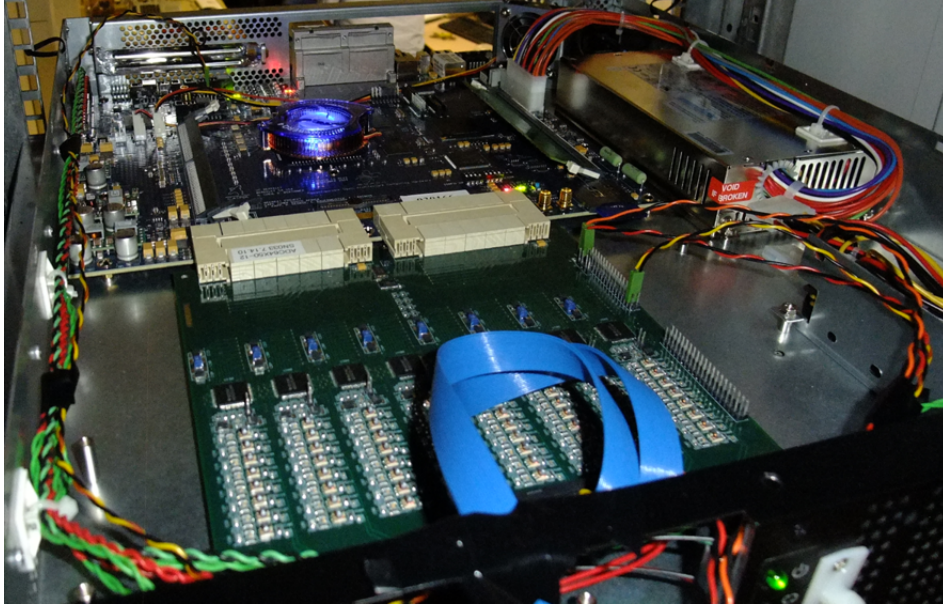
Figure 2. The 'f-engine' ROACH board, a Virtex 5 SX95T FPGA board, with the 64 input ADC connected via two Z-DOK connectors.

Digital Backend Specifications		
Digitizer/Channelizer (F-Engine)		
ADC Sampling Rate	40	MHz
ADC Sampling Precision	12	bit
Antenna-polarizations	32	single pol
PFB	4 tap FIR + 2048 point FFT	Radix-2 Biplex Real FFT
Quantization	4	bit
FX Correlator (X-Engine)		
Auto Correlations	32	
Cross Correlations	496	
Minimum Integration Length	6.55	ms
Output	10 GbE	SPEAD protocol
Spatial FFT Imager (S-Engine)		
2D FFT	8 x 16	
Beams	128	
Minimum Integration Length	1	s
Output	1 GbE	SPEAD protocol
Beamformer Output	10 GbE	Up to 8 Beams

Table 2. A three ROACH design where the correlator and spatial FFT imager use the digitizer/channelizer interface.

2.1 Digitization and Channelization

Signal digitization is performed using the Texas Instruments ADS5272 8 channel, 12 bit ADC. The ADC board, developed by Rick Raffanti [3], uses eight of these ADCs to channelize 64 streams at up to 65 Msps. In our design only 32 signal streams are digitized at 40 Msps which covers the 16 MHz analogue band. The ADC is clocked with a 160 MHz clock which is locked to a local maser source. During the analogue stage the RF, centered at 408 MHz, has been mixed down to baseband. Prior to digitization the last amplifier stage of the analogue chain has per signal adjustable gain useful for setting levels for ADC

[3] https://casper.berkeley.edu/wiki/64ADCx64-12

| F-Engine ROACH Resource Utilization (Virtex 5 SX95T)		
ADC Clock	40 MHz	
System Clock	160 MHz	Demux:4
Slice Registers	30217 / 58880	51%
Look Up Tables	24319 / 58880	41%
BRAM (36kb)	205 / 244	84%
DSP48e (Multipliers)	185 / 640	28%
CX-4 Interface	2 / 4	5.12 Gbps XAUI
QDR Memory	2 / 2	Cornerturn

Table 3. DSP implementation of the f-engine ROACH board
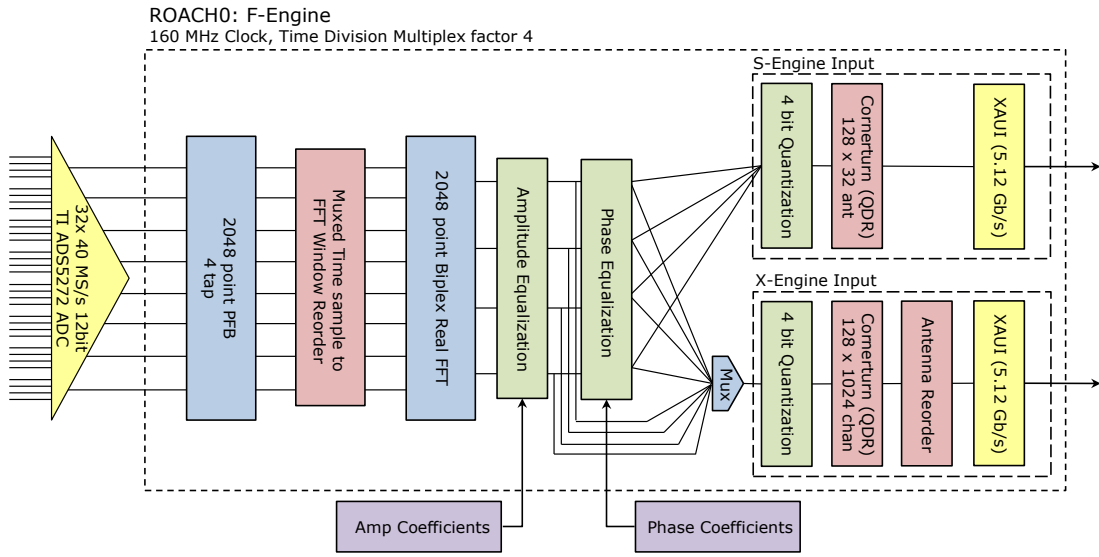
Figure 3. During observations amplitude and phase coefficients are applied to scale the power for the 4 bit correlation and apply phase corrections for the spatial FFT.

quantization. This ADC is connected via a dual Z-DOK interface to an 'F-Engine' ROACH which performs the channelization. A block diagram of the design layout is shown in figure 3.

The ROACH board is clocked at four times the sample rate such that four signals are time division multiplexed onto a single stream. Channelization is performed with a four tap Hann filter, 2048 point polyphase filterbank (PFB) to produce 1024 samples per real antenna stream. The CASPER PFB has been modified to account for the signal multiplexing. Each channel has a width of 19.5 kHz and the output of the FFT stage is a 36 bit complex number. The narrow channel widths and PFB windowing allows for good frequency separation in the high RFI environment at the observatory. After channelization the samples are quantized down to 8 bit complex. An adjustable, per channel complex gain equalizer is used for amplitude and phase corrections before quantization. Complex gain calibration is essential to proper spatial FFT imaging which must be applied before the spatial FFT. The FX correlator is used to generate calibration coefficients which are applied back into the equalizers. A selectable mux is available to skip the phase coefficients on the FX correlator data stream. Post equalization, the data stream is split in two for specific reordering for the correlator and imager. The correlator data stream is reordered to 128 time samples for a single antenna for a single frequency channel. Followed by the next antenna and cycles back onto the next frequency channel. The imager takes in one time sample of each antenna for a given frequency channel and cycles through 128 time samples before stepping to the next frequency channel. After data reordering each stream is sent over high speed XAUI at a rate of 5.12 Gbps to the correlator and imaging boards. The FPGA resource usage is listed in table 3. There is suffcient resources to include additional features in the 'F-Engine', i.e. finer channelization, increase in antennas, increase in bandwidth.

Pipelined X-Engine
N time sample per antenna, M antennas
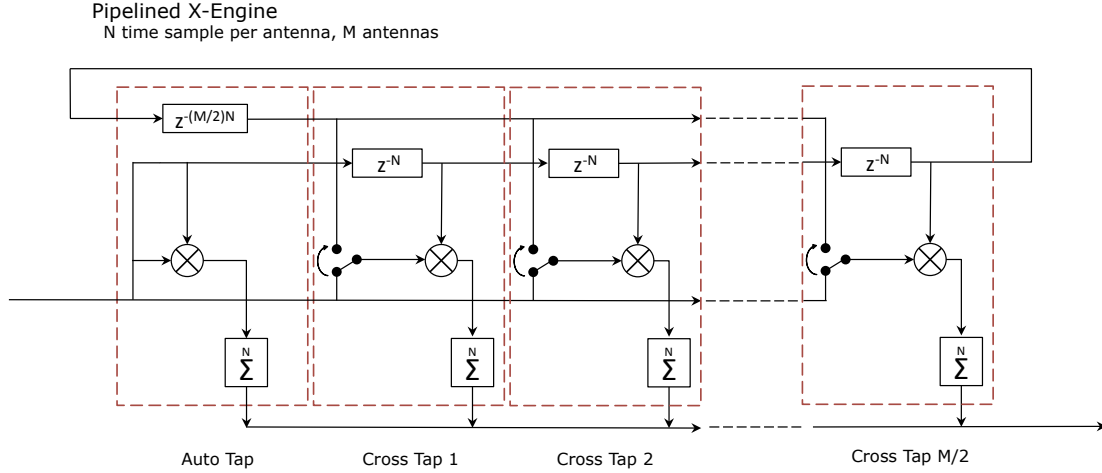
Figure 4. The input is ordered as N time samples per antenna per frequency channel. An accumulation stage after the complex multiply reduces the data rate of each tap. Outputs are multiplexed onto the same output using a valid signal.

2.2 FX Correlator

An FX correlator design is a standard design for large bandwidth and many antenna arrays. The F component represents the frequency channelization, and the X is a complex multiply and accumulate (CMAC). An overview of the architecture is presented in (Parsons et al. 2006). Architecture efficiency goes as $O(M\log M) + O(N^2)$ where M is the number of FFT frequency channels and N is the number of antenna-polarizations. The core component to the X stage of the FX correlator is the complex multiplication of all pairs of independent signals for each frequency channel. A pipelined x-engine, based on the general CASPER block originally designed by Lynn Urry(Urry et al. 2007), is used for multiplier efficiency. The pipeline design is constructed out of $M/2$ 'taps' where the ith tap computes the correlation between antennas A_j and A_{j+i} for every antenna A_j of M total antennas. To maximize the multiplier usage a loopback is added to use every i^{th} tap to compute the correlation of antennas A_j and $A_{M/2+j+i}$, fig. 4. Each tap accumulates for N time samples to reduce the output data rate.

An asynchronous architecture is used between the f-enigne and x-engine boards. The x-engine board has been clocked to 200 MHz, well above the 160 MHz f-engine board, this assures the x-engine board will never have input buffer overflows during the windowing stage. The XAUI interboard connection is a streaming interface which guarantees the same output order as input order but with variable latency. In rare cases the XAUI interface can drop 64 bit words during the streaming, this requires an initial stage to track the number of words received between headers. In case of missing words the entire payload is dropped and counters reset for the next header. A correlation is only performed on a per channel basis. The channelized band can be split up into portions and processed in parallel across multiple x-engines. This allows a larger bandwidth to be processed at the cost of increased logic and multiplier resource utilization. We currently under utilize the avalible resources on the FPGA, table 4. For this design two pipelined x-engines are used which each processes half of the band, figure 5.

The x-engine design requires a continuous stream of data for 128 samples of all antennas for a single frequency channel. Prior to the x-engine samples are buffered up into windows to guarantee valid data during a cycle of the x-engine. For reasons related to the design the 32 single polarization signals are treated as 16 dual polarization signals. This causes a small number of redundant baseline correlations and a conjugation effect which is corrected in post processing. During the x-engine stage an initial accumulation of 128 sample is performed after the complex multiply to reduce the output rate to roughly the input rate. This limits the minimum integration time to 6.55 ms. In addition to the standard CASPER pipelined x-engine design an optimized version has been tested. This new optimized design efficiently uses the full bit width of the Xilinx DSP48 multipliers to reduce the total multiplier usage by a 75%. A description of this optimized design is in preparation.

A vector accumulator using the on board QDR memory is used for longer integration lengths. This second accumulator is software controlled with integration lengths ranging from milliseconds to minutes. A completed integration is sent to a receive computer over a 10 GbE connection. Integrations are split up based on the SPEAD protocol[4] and transmitted as UDP packets.

[4] https://github.com/ska-sa/PySPEAD

X-Engine ROACH Resource Utilization (Virtex 5 SX95T)		
System Clock	200 MHz	
Slice Registers	28494 / 58880	48%
Look Up Tables	25349 / 58880	43%
BRAM (36kb)	88 / 244	36%
DSP48e (Multipliers)	288 / 640	45%
CX-4 Interface	1 / 4	5.12 Gbps XAUI
QDR Memory	2 / 2	Vector Accumulator

Table 4. DSP implementation of the x-engine ROACH board.
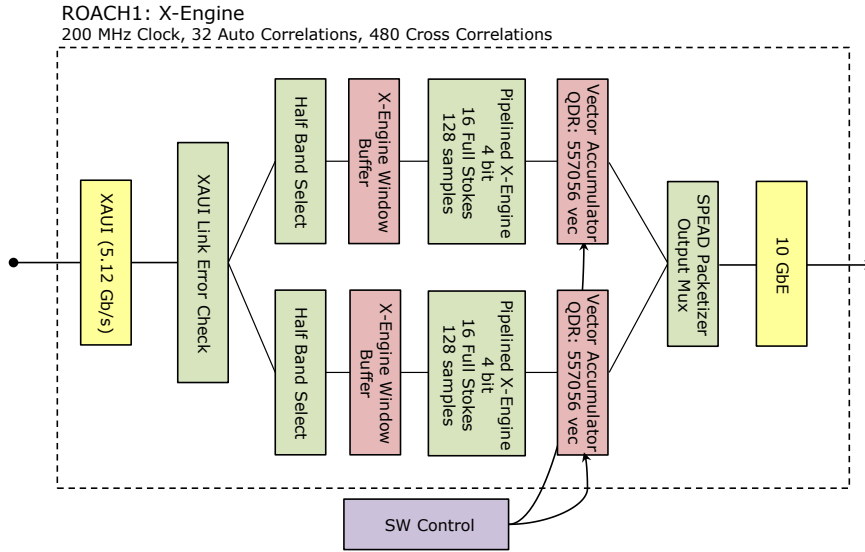
Figure 5. Two parallel pipelined x-engines are used, each processes half of the band.

2.3 Spatial FFT

When N receiving elements in an antenna array are placed on a regularly spaced grid, a well known method for producing a complete set of orthogonal beams on the sky is the spatial fast Fourier transform (Williams 1968). Such a beamforming implementation will generate N beams on the sky, with a computational cost of $O(N \log N)$. For large arrays, where many beams are desired, this can be a significant computational saving, with the alternative, so-called *DFT beamforming*, requiring $O(N)$ operations per synthesized beam. To date, the largest such astronomical implementation of such a spatial fast Fourier transform beamformer is the 64 element dish array constructed in 1994 at Waseda University, Japan (Otobe et al. 1994).

More recently, spatial FFT based processing has been revisited in the literature with an emphasis on the correlation matrix, rather than the collection of beams, as the mathematical object of interest (Tegmark & Zaldarriaga 2009) (Tegmark & Zaldarriaga 2010). In the method outlined by Tegmark & Zaldarriaga, zero padding is applied to the matrix of antenna signals before the spatial FFT is performed, and as such, the complete set of visibilities for all unique baselines in the array can be obtained, post integration, by inverse Fourier transform. Conversely, in the image plane, the zero-padding required by the prescribed algorithm results in the generation of $2^m N$ beams on the sky and is dependent on the number of dimensions, m, in the antenna array. Regardless of potential downstream visibility domain processing, this oversampling of the sky by a factor 2^m has the benefit of increasing the instantaneous uniformity of sky coverage by synthesized beams, which somewhat alleviates the limitations associated with the inability to steer multiple beams independently.

In the BEST-2 backend described here, the requirements on the spatial FFT processor were multifold. Firstly, the system should be capable of generating images on an O(second) timescale, by the method described by (Tegmark & Zaldarriaga 2009). Further, the system should be capable of passing formed beams at full bandwidth, i.e. without any accumulation, to downstream time domain processing systems such as the real-time pulsar dedispersion engine (Magro et al. 2011).

This redundancy for the BEST-2 array is show in figure 6. Instead of making individual correlations of the same baseline as in an FX correlator the correlation of the average of each baseline can be computed. This optimization relys on the
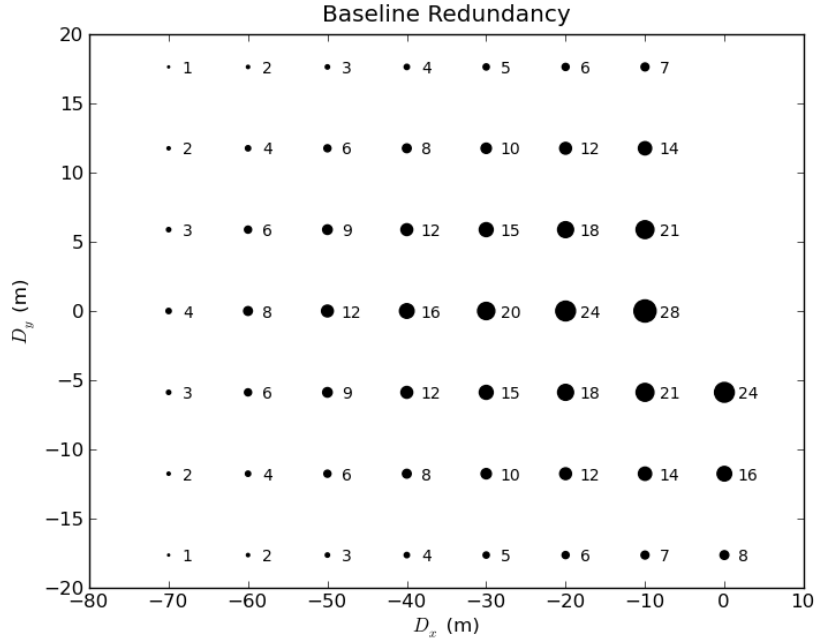
Figure 6. A 4 by 8 regularly gridded array has 53 unique baselines, 480 cross correlations are performed. The number of redundant baseline measurements is shown as the color and size of each circle.

assumption that each redundant baseline measurement is indeed identical. Thus any calibration to the complex gains must be applied before the spatial FFT.

Though the X-Engine and S-Engine use the same F-Engine each requires a unique data windowing order. For the S-Engine a window is made up of N antennas by M time samples for a given frequency channel. A similar XAUI interface and windowing scheme is used as in the X-Engine which buffers up windows of valid data to stream into the spatial transform. The 2D spatial transform is performed using an 8 point FFT followed by a cornerturn and 16 point FFT. A block diagram of the design layout is shown in figure 7. The BEST-2 array is a grid of 4 by 8 antennas, the data is zero padded before input into the 8 by 16 point spatial transform. A 4 by 8 point spatial transform will only produce gain information for each spatial position, which can be interpreted as an array of beamformers covering the field of view. This zero padding is necessary to produce both the gain and phase information of each spatial position which is an effective baseline. Each effective baseline is an average of all possible baselines with the same spatial dimensions. The four fold increase is the number of outputs from the spatial transform by double padding introduces a number of redundant calculations. The spatial transform produces 128 outputs. There are only 53 unique baselines in a 4 by 8 grid. The datarate out of the S-Engine is reduced by a two stage vector accumulator. A fixed 128 sample vector accumulator reduces the output of the second stage FFT so that the 1024 channels of the 128 computed spatial components can be multiplexed onto one line and accumulated in a software controllable QDR vector accumulator. Accumulations are sent out over the 1 GbE PowerPC interface using the a SPEAD UDP packet format. Individual beams can be selected out before accumulation and sent over 10 GbE in a LOFAR beam packet format which will be used for future pulsar processing.

3 DEPLOYMENT AND INITIAL OBSERVATIONS

Instrumentation was installed and tested over a two week period in March 2012. During that time a number of test signals were used to check the system status. Various bright radio sources were observed once the analogue and digital systems were checked out. Since the Northern Cross is a transiting array there is a limited period of time each day in which a source is in the primary beam. Bright sources such as Cygnus A, Cassiopeia A and Taurus A along with a number of 3C sources were observed along with multiple constant declination 24 hour cycles.

Raw data from the correlator and imager was recorded to HDF5 files using a SPEAD protocol receive script. A suite of python scripts have been written to interface and manipulate the data in this pre-calibration stage. A python FITS-IDI
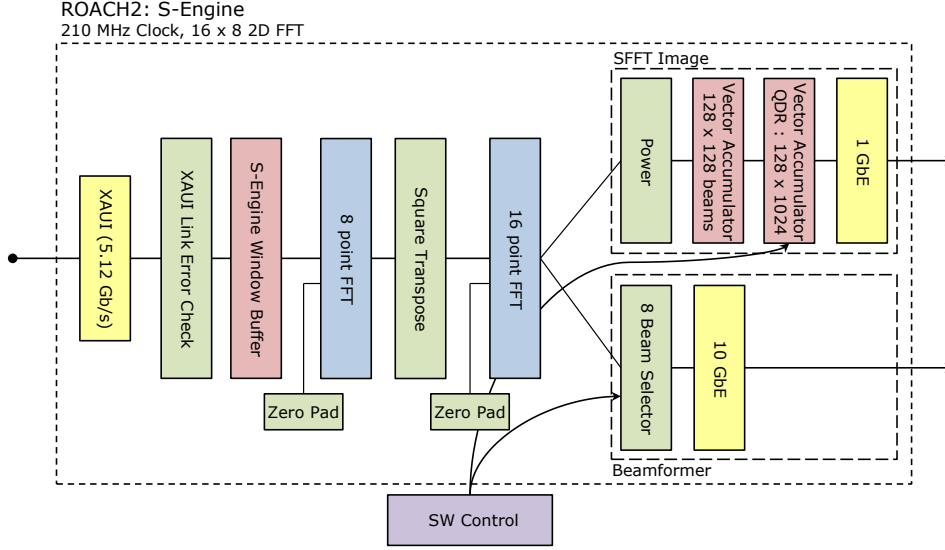
Figure 7. During the two stage spatial FFT the streams are zero padded to provide phase information of each baseline.

package has been written to convert HDF5 files into the standard FITS format which can be read by AIPS and CASA[5]. This allows for conversion to the Measurement Set format which most packages can interface with.

3.1 FX Correlator Imaging

During observations no phase tracking is applied to the antennas. The integration time is sufficently short that this does not effect the phase. This allows the array to be phase tracked to any position in post processing. Before conversion to measurement sets a phase center is chosen and a phase correction is added to each integration. We are limited to a fixed observation length per day for a given source. The UV coverage is essentialy the same for any observation, with some variation due to pointing declination.

The East-West full width half max (FWHM) beam size of an individual element is $\approx 11.25°$ which translates to a 45 minute 'transit time' for a source, as seen in the measured primary beam, figure 8. For the the bright A class sources this time can be extended since they remain the dominating source well after crossing the FWHM. Observations of 80-90 minutes are possible which gives an small improvement in uv coverage at the cost of properly accounting for the amplitude modulation due to the primary beam. This warrants a small sensitivity benefit for a large calibration cost. Most images are created using data within a few minutes of the source transit time. The high sidelobes in the primary beam, figure 8, cause the bright class A sources to dominate even when they are far from the field of view and makes it difficult to perform calibration and imaging near these sources.

A transiting array provides a unique challenge of gain calibration since a source's apparent gain will change as it transits the primary beam. To account for this a two stage gain calibration method is used. Phase calibration and setting the flux scale is accomplished using Casseiopia A and Cygnus A observations as point source sky models set to their 3C flux levels and known spectral indices. Since these sources are very bright, only a few seconds at transit is needed produce a high SNR dataset to use for calibration. Over this period the primary beam can be approximated as flat. A time independent complex gain is derived for a coarse calibration. After applying the gain corrections an observation will be set to a flux scale relative to the flux of the calibration source. Each individual source is then self calibrated in MeqTrees(Noordam & Smirnov 2010) based on a local sky model taken from the 3C catalog. This stage is calibrated on short time intervals to account for amplitude changes from the primary beam.

An effect of the density of the antenna layout is a low point spread function(PSF) to field of view ratio (spatial fidelity), thus images tend to contain at most a few spatial seperate point sources. The grid layout of the BEST-2 array produces strong sidelobes and grating lobes in the PSF as seen in figure 9b. Observations of bright point sources produces calibrated dirty images in which the PSF is clearly visible, fig. 9c. After cleaning we measure the residual noise to be around 2 Jy over a number of two minute snapshot observations, table 5. Imaging using longer source transit times has shown the noise floor

---

[5] https://github.com/telegraphic/pyfitsidi
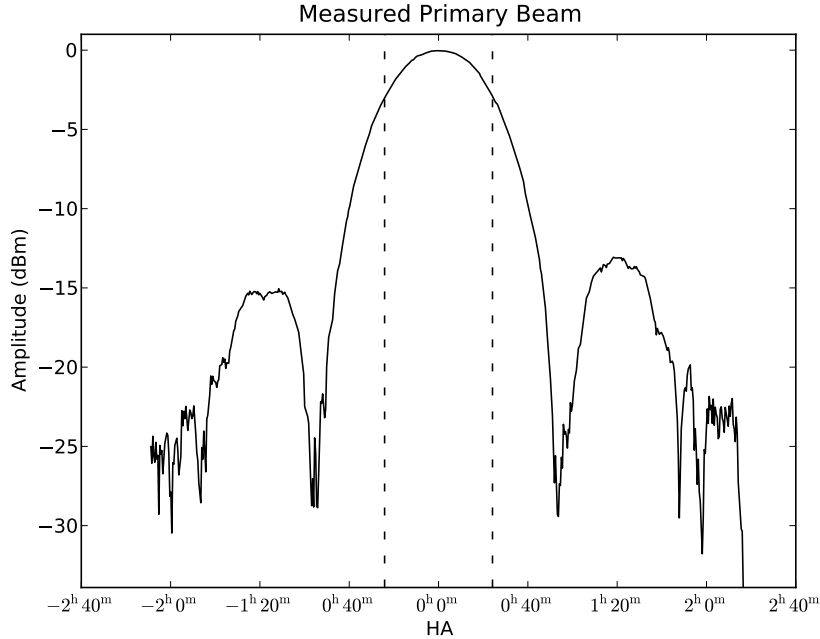
Figure 8. A measured east-west primary beam based on the correlation between antennas 1N-6-1 and 1N-1-3, which are representitive of typical antennas, based on a Cassiopeia A transit. The dashed lines indicate the FWHM points. The antennas should have a sinc response to a point source, as expected the first sidelobes are -15 dB down from the peak.
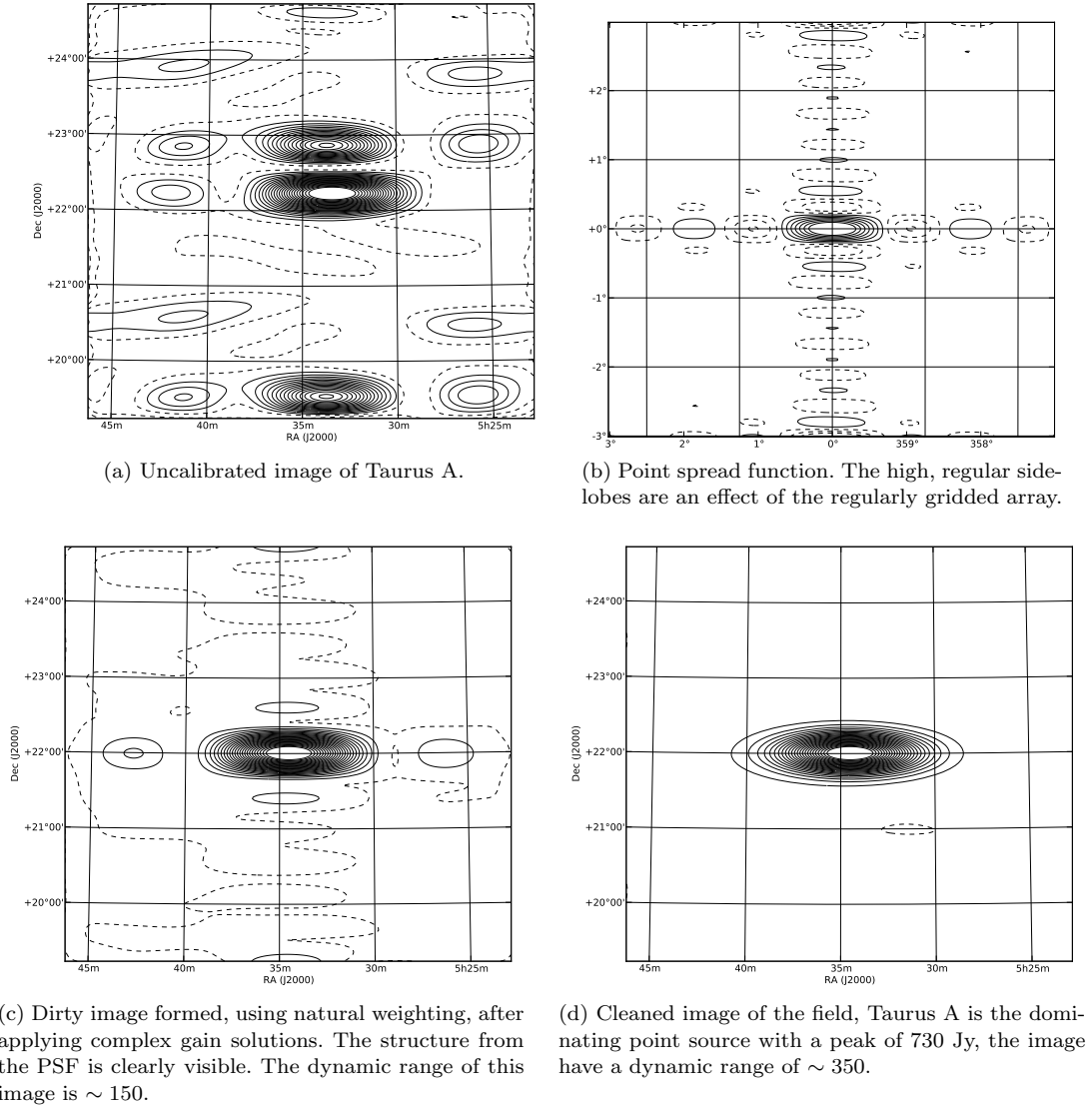
to decrease at the expected rate. The various stages of imaging an calibration for the source Taurus A is shown in figure 9. Further images and analysis of the data quality are followed in section 4.

3.1.1   Solar Observation during Highly Active Period

During calibration observations of Cassiopeia A a second source was found in the field. The second source had approximately the same peak flux as Cassiopeia A and initially though to be a problem in the observation. But it was shown to appear in multiple observations of the field and the source appeared to change position each day. It has been determined that this second source was the Sun. At the time of our observations, March 2012, the Sun was at a similar sidereal time as Cassiopeia A. Also, in that time the Sun was undergoing a very active period which maybe one of the reasons we observed it at with a particularlly strong flux. Even though the Sun was at a declination of approximately $-4°$, over $60°$ way from Cassiopeia A, the source appears in the same field. A combintation of high primary beam sidelobes and an active solar period led to the sun being detected $62°$ away from it's actual position. The sun is approximately a half a degree in size, the longest north-south baseline is on the order of the same size and we begin to resolve the sun in that direction. Figures 10a and 10b show the Cassiopeia A field seperated by 10 days, in that time the sun has moved well into the center of the field. This made using Cassiopeia A as a calibration source not possible during our initial observations.

3.1.2   Weighting for a Regularly Gridded Array

As noted, the regular gridded array produces many highly redundant baselinesi, fig. 9b. When forming the dirty image the choice of weighting greatly effects the outcome of the image. In the highly redundant array case of BEST-2 the effects of using uniform versus natural weighting can be seen in fig. 11. The uniform weighting scheme significantly reduces the sensitivity the image for a small improvement in spatial resolution. We have used a natural weighting scheme through out to produce images. It is worth noting that the baselines produced by the spatial FFT instrument have an inherent 'natural' weighting scheme since all redundant baselines are effectively summed together into a single baseline. To change the weighting of the spatial FFT baselines reweighting factors must be added to the data based on how redundant each baseline is.

(a) Uncalibrated image of Taurus A.

(b) Point spread function. The high, regular side-lobes are an effect of the regularly gridded array.

(c) Dirty image formed, using natural weighting, after applying complex gain solutions. The structure from the PSF is clearly visible. The dynamic range of this image is ~ 150.

(d) Cleaned image of the field, Taurus A is the dominating point source with a peak of 730 Jy, the image have a dynamic range of ~ 350.

Figure 9. Images and PSF formed from an FX correlator two minute snapshot observation of Taurus A.

4 SPATIAL FFT RESULTS AND COMPARISON TO THE FX CORRELATOR

4.1 Calibration Methods

The effective averaging of redundant baselines in the spatial FFT imager requires complex gain calibrations to be applied during observations. To derive gain coefficients a calibration method is applied to the FX correlator data. In initial observations the column ratio gain estimation method from (Boonstra & Veen 2001) was used to compute a per channel, per antenna complex gain terms.

In the ideal case, observations using the spatial FFT will be identical to observations using an FX correlator. The ability to solve for independent complex gain terms post observation is not possible with the spatial FFT. Calibration must therefore be applied in real time during the observation. Deriving the complex gain terms to be applied to the antennas can be achieved with any desired calibration method. But time dependent variations in complex gains introduce errors phase and amplitude errors into baselines.

4.2 Spatial FFT as a Beamformer

4.3 Spatial FFT as a Correlator

The output image data from the spatial FFT can be converted to uv sampled baselines by performing an inverse FFT. All redundant baselines are combined into a single unique baseline which makes pre-measurement calibration essential to producing a good observable. In total 52 unique baselines are produced along with the auto correlation. Each unique spatial
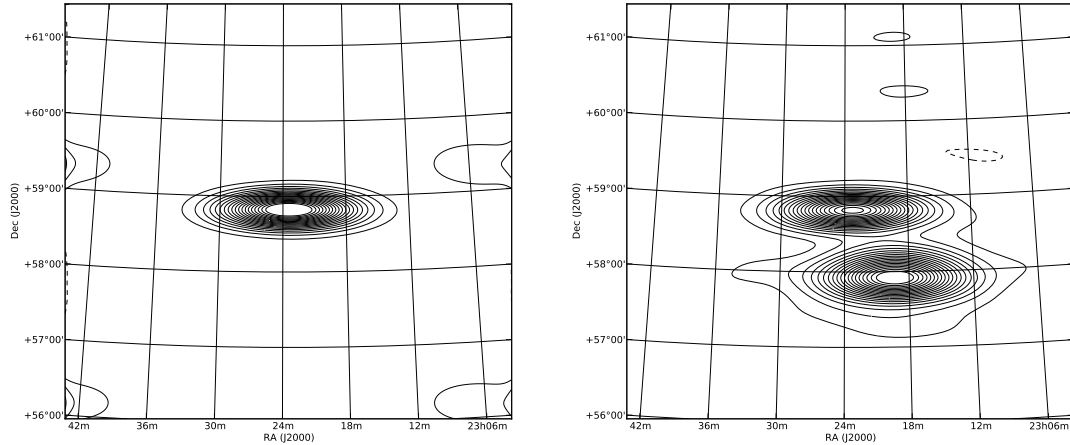
(a) Observation of the Cassiopeia A field on Julian Date 2455985, the flux has been fixed to 5600 Jy with a dynamic range of ~ 900. The structure on the edge of the image are likely from the sun begining to come into the field of view.

(b) Observation of the same field ten days later on Julian Date 2455996. The Sun is slightly resolved in the North-South direction. The Sun is at declination $-4°$, about $62°$ from the field of view but is within one of the primary beam sidelobes and has an apparent declination position at $58°$. Using the same flux scale from the previous Cassiopeia A observation the Sun is measured to have a flux of 6000 Jy. Though, the Sun is being observed through a sidelobe this value is attenuated compared to the actual value.

Figure 10. Images of the Cassiopeia A field at different Julian dates show the Sun appearing in a primary beam sidelobe.
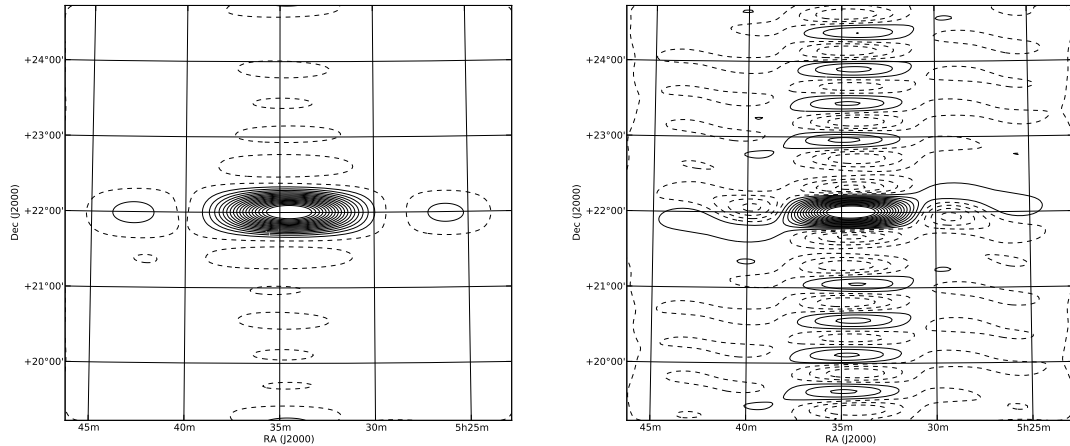

(a) Dirty image with natural weighting of the point source Taurus A.

(b) Dirty image with uniform weighting of the point source Taurus A.

Figure 11. Natural versus uniform weighting of a point source.

FFT baseline is a linear combination of antenna pair baselines at the same uv position. Once in the baseline correlation format the same pipeline that is used for the FX correlator is used to convert the data into measurement sets.

Antenna gain calibration can not be performed on the spatial FFT correlations since each baseline is made up of a linear combination of redundant baselines. Thus no calibration is applied to the output data. The flux scale is set by using the flux scale from the FX images. This scale can be set during the observation or in post processing since it is a baseline independent amplitude scaling. The figures 13a and 13b show the dirty and clean images of Taurus A during a properly calibrated observation. The signal to noise of the images are comparable to that of the images formed with the FX correlator during the same observation, fig. 9. We expect both instruments to produce comparable results, though there has been an open question as to how 'good' the real time calibration must be and how often this calibration must change. In the following section we look at the results of observations from both instrument to understand to the quality of images produced by the spatial FFT relative to that of the FX correlator.
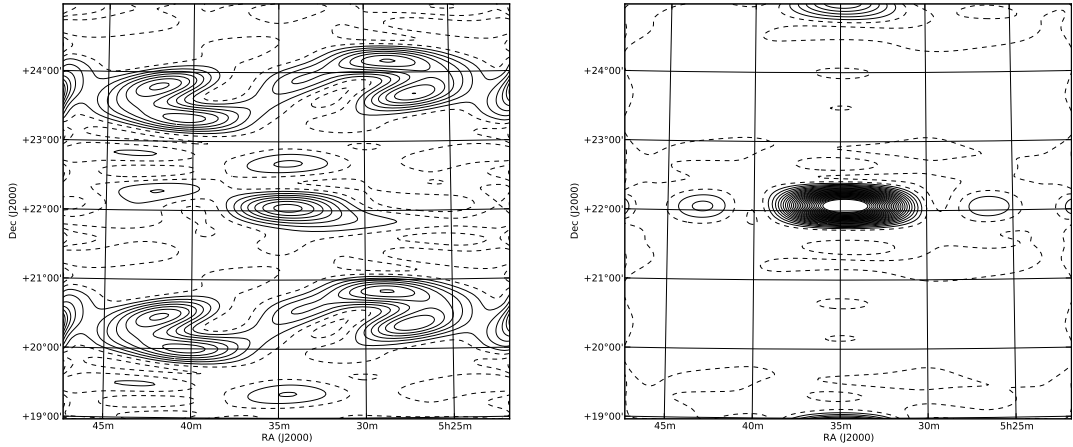
(a) Dirty image of Tau/3c144 formed before applying complex gain calibrations in the F-Engine for the spatial FFT. The uncalibrated phases spread the power through out the image.

(b) Dirty image of Tau/3c144 with complex gain calibrations applied. This image has a signal to noise ratio around 100, a standard CLEAN method can be used to improve the image dynamic range.

Figure 12. After applying complex gain calibration a bright point source such as Tau/3c144 appears similar to the array PSF, and has a significant improvement in the image fidelity compared to the uncalibrated image.
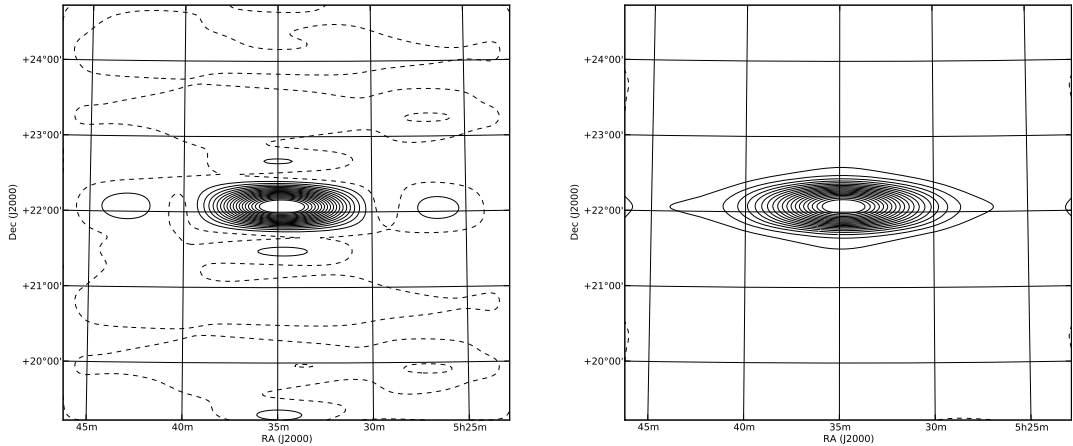
(a) Dirty image of Taurus formed from the spatial FFT imager, the flux scale has been fixed to the scale based on the same image from the FX correlator. The dynamic range,∼ 100, is less than that of the FX correlator image, ∼ 150.

(b) Cleaned image of the Taurus field. The cleaning process brings the dyanmic range up to around 300, similar to the value from the FX correlator image in fig. 9d. A notable feature about the the cleaned images from the spatial FFT is the apparent low level skewing of the image, particularly in the east-west direction.

Figure 13. The images produced by the spatial FFT imager are comparable in noise and dynamic range to those produced with calibrated FX correlator data.

4.3.1 Image Comparison

In the spatial FFT images there is a noticable distortion of point sources. The cleaned image of Taurus, fig. 13b, begins to form points at the low levels, primarily in the east-west direction. This effect can also be seen in a number of the 3C images in figures 14 and 15. This effect is not noticable until the image has been cleaned. The variation in antenna phases is probably the primary factor causing the distortion.

To make a comparison between images we define the dynamic range of each image to the peak flux divided by the standard deviation of the noise in a empty region of the image. Selecting an empty region of an image can greatly influence the dynamic range if there is low level structure, we took care to select a few regions per image to select a representative region. The same region would then be used for images from both the FX correlator and the spatial FFT imager as to avoid bias. Though this is a simple way to define an determine the noise level and dynamic range we are not interested in the absolute flux of the images. We are interested in the difference in image quality between the two sets of results. In table 5 we list a

Measured Source Flux and Noise Levels

Source	3C Flux (Jy)	Peak Flux (Jy)	FX Noise Level (Jy)	SFFT Noise Level (Jy)
3C10	134	67.2	1.1	1.3
3C48	47	27.3	0.9	0.8
3C123	175	91.1	2.1	1.9
3C144	1420	729.5	2.0	2.5
3C157	210	116.5	1.6	2.3
3C196	59	34.6	0.9	1.7

Table 5. Noise level for various 3C sources calculated for images formed with data from the FX correlator and the spatial FFT imager.

number of 3C sources along with their measured flux and noise levels. For these snapshot images the spatial FFT produces essentially the same results as the FX correlator.

The dynamic range of the spatial FFT appears to be approximately the same as the FX correlator but there is a low level distortion in the spatial FFT images in a few of the sources. To understand this we can look at the baseline data to see how that varies between the two measurements.

4.3.2 Baseline Phase Comparison

With an FX correlator a 'bad' baseline or antenna can be flagged in the data during post processing. If each baseline has an nominal phase noise of σ_{nom} then a 'bad' baseline can be defined as having a noise level of N times higher than the nominal noise level, $N\sigma_{nom}$. For a spacing with m redundant baselines the combined noise is $\sigma_{bl} = \sigma_{nom}\sqrt{m}$. If there are B bad baselines which are flagged the noise becomes $\sigma_{bl} = \sigma_{nom}\sqrt{(m-B)}$. In the case of the spatial FFT all the baselines are summed together before a baseline can be flagged. Then the baseline noise is $\sigma_{bl} = \sqrt{m-B}\sigma_{nom} + \sqrt{B}N\sigma_{nom}$. If a subset of the antennas are malfunctioning during an observation they corrupt any spatial FFT baseline they are part of. It should be noted that in the case of a known bad antenna, that antenna can be flagged during an observation and dropped.

5 DISCUSSION

REFERENCES

Boonstra A. J., Veen A. J. V. D., 2001, in IEEE Workshop on Statistical Signal Processing (SSP), IEEE

Magro A., Karastergiou A., Salvini S., Mort B., Dulwich F., Zarb Adami K., 2011, MNRAS, 417, 2642

Montebugnoli S., Bartolini M., Bianchi G., Naldi G., Manley J., Parsons A., 2009a, in Proceedings of Wide Field Astronomy & Technology for the Square Kilometre Array (SKADS 2009). 4-6 November 2009. Chateau de Limelette, Belgium, pp. 355–358

Montebugnoli S., Bianchi G., Monari J., Naldi G., Perini F., Schiaffino M., 2009b, in Proceedings of Wide Field Astronomy & Technology for the Square Kilometre Array (SKADS 2009). 4-6 November 2009. Chateau de Limelette, Belgium, pp. 331–336

Noordam J. E., Smirnov O. M., 2010, A&A, 524, A61

Otobe E. et al., 1994, Publications of the Astronomical Society of Japan, 46, 503

Parsons A. et al., 2006, in Asilomar Conference on Signals and Systems, Pacific Grove, CA, pp. 2031–2035

Perini F., 2009, in Proceedings of Wide Field Astronomy & Technology for the Square Kilometre Array (SKADS 2009). 4-6 November 2009. Chateau de Limelette, Belgium., pp. 341–345

Perini F., Bianchi G., Schiaffino M., Monari J., 2009, in Proceedings of Wide Field Astronomy & Technology for the Square Kilometre Array (SKADS 2009). 4-6 November 2009. Chateau de Limelette, Belgium, pp. 351–354

Tegmark M., Zaldarriaga M., 2009, Phys. Rev. D, 79, 083530

Tegmark M., Zaldarriaga M., 2010, Phys. Rev. D, 82, 103501

Urry W., Wright M., Dexter M., MacMahon D., 2007, ATA Memo: The ATA Correlator. Tech. Rep. 73, University of California, Berkeley

Williams J. R., 1968, The Journal of the Acoustical Society of America, 44, 1454
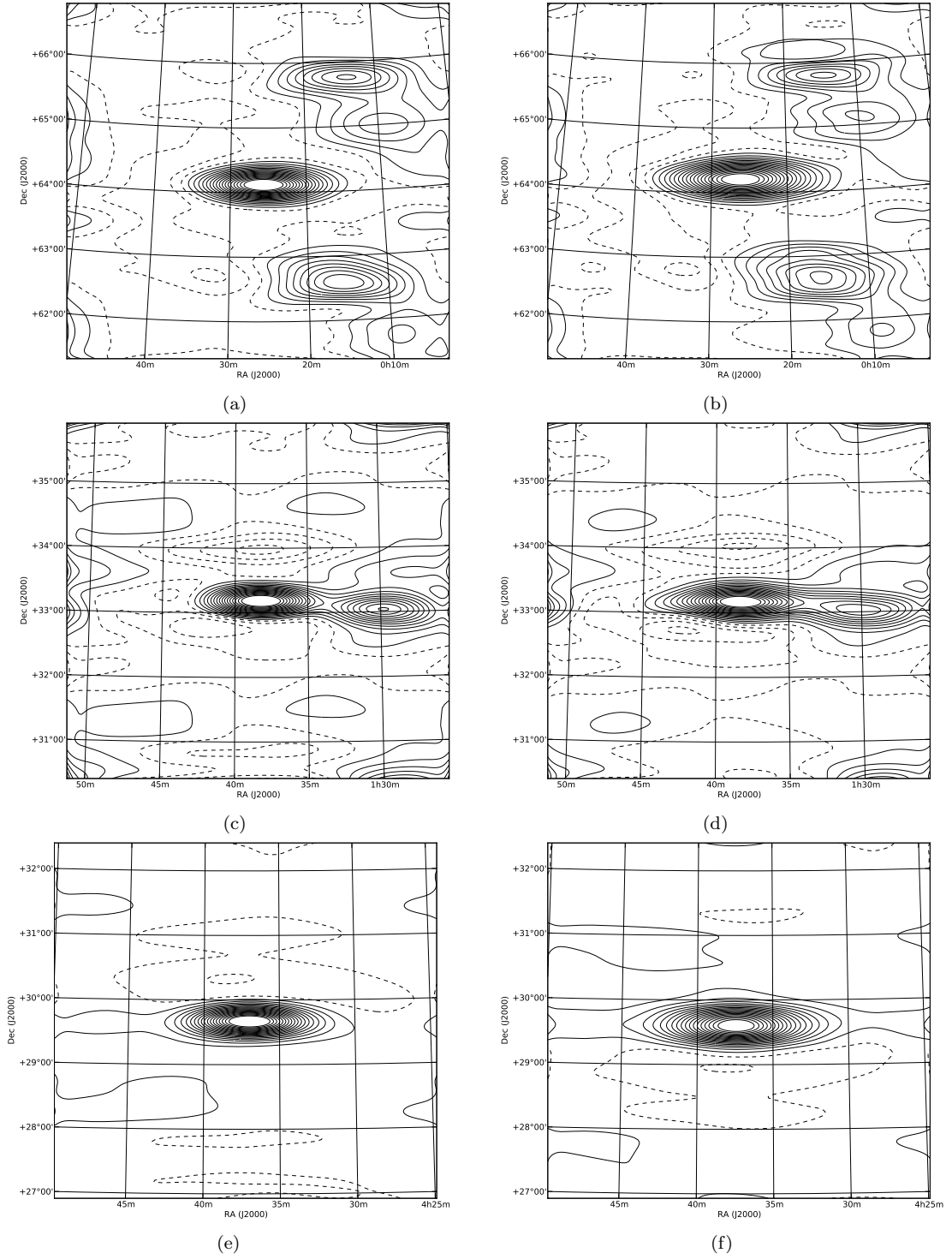
Figure 14. Cleaned images formed from simultaneous observation of various sources with the FX correlator and spatial FFT imager. The left column is from FX correlator data, the right column is spatial FFT data. Sources are 3c10 (fig. 14a,14b), 3c48 (fig. 14c,14d), 3c123 (fig. 14e,14f). The FX correlator and spatial FFT images have comparable noise floors of about 2 Jy in all images and difference in dynamic range varying from a few percent to 10 percent depending on the source.
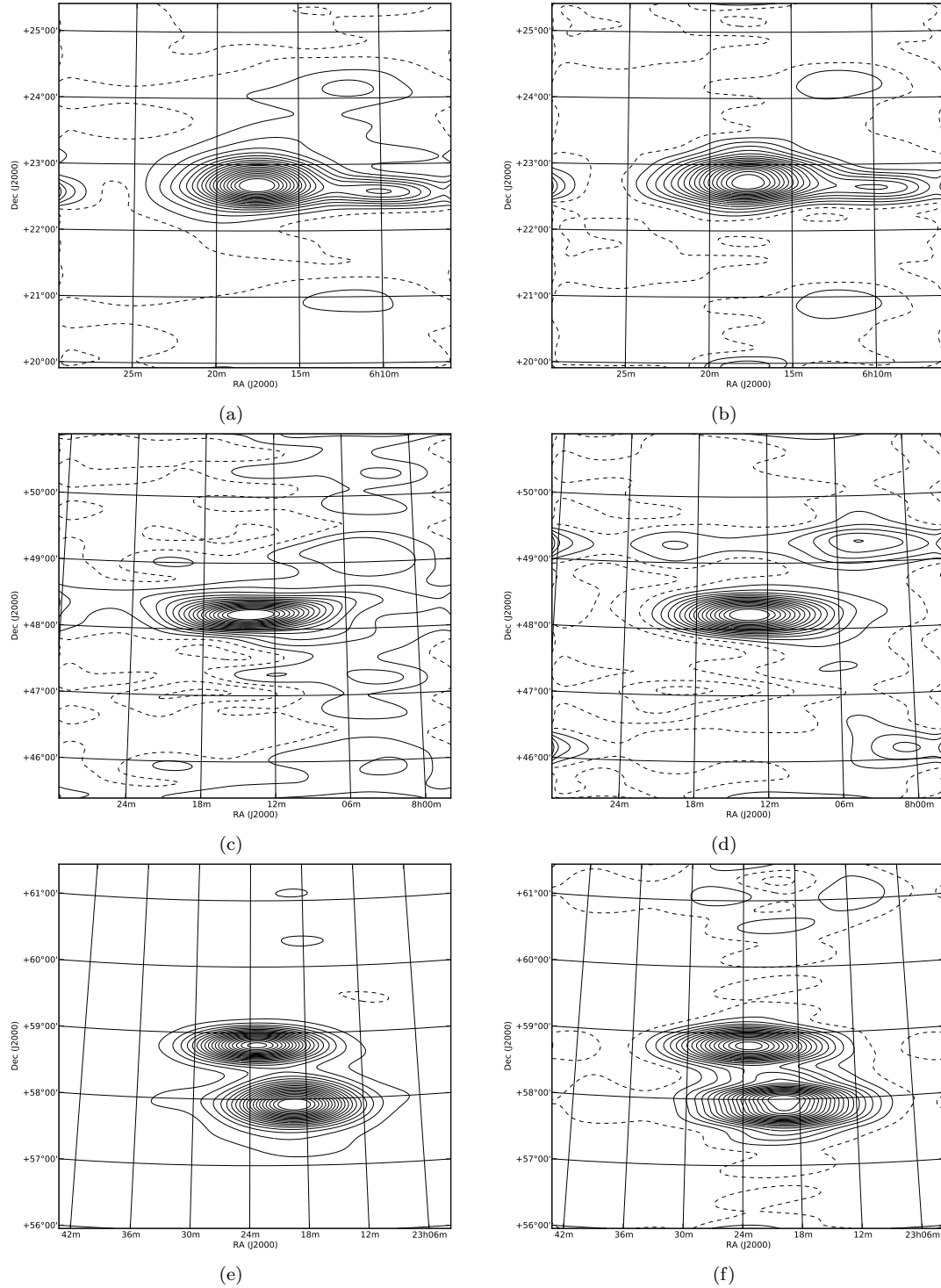
Figure 15. Cleaned images formed from simultaneous observation of various sources with the FX correlator and spatial FFT imager. The left column is from FX correlator data, the right column is spatial FFT data. Sources are 3c157 (fig. 15a,15b), 3c196 (fig. 15c,15d), Cassiopeia A with the sun in a sidelobe (fig. 15e,15f). The FX correlator and spatial FFT images have comparable noise floors of about 2 Jy in all images and difference in dynamic range varying from a few percent to 10 percent depending on the source.
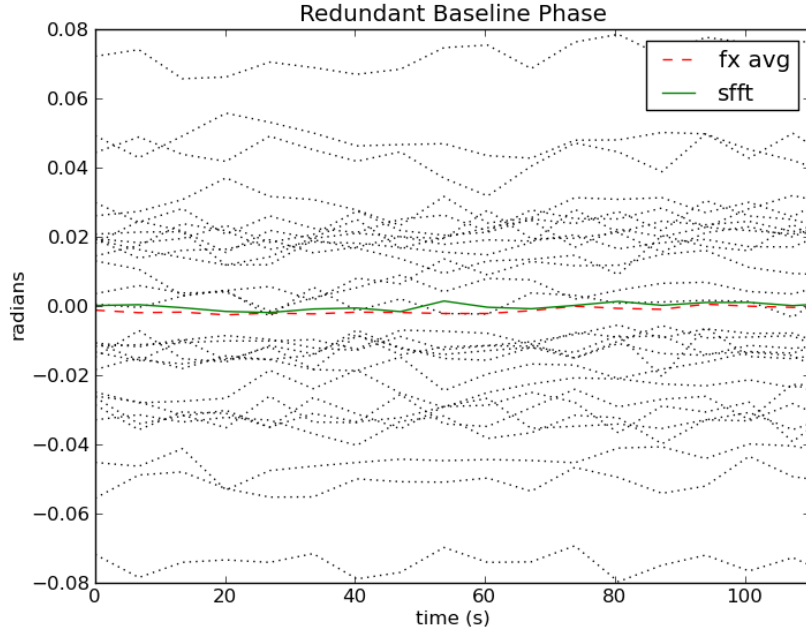
Figure 16. Phase comparison of the FX correlator baselines which are redundant with the (0,4) antenna spacing and the corresponding spatial FFT baseline. The lines are: redundant FX correlator baselines(dotted), spatial FFT combined baseline (solid), all the FX baselines averaged together(dashed). For this baseline, the spatial FFT baseline fits the averaged FX baseline well but has $\sim 35\%$ more noise.
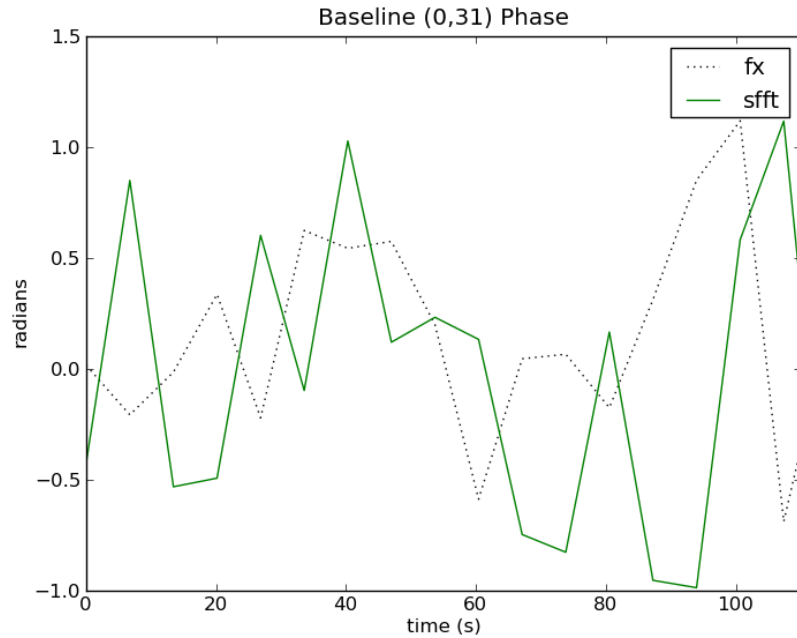
Figure 17. The (0,31) baseline is the one of the non-redundant baselines in the array. Both instruments should produce a baseline with similar noise characteristics. But the standard deviation of the noise from the spatial FFT observation is 48% higher than the FX correlator.
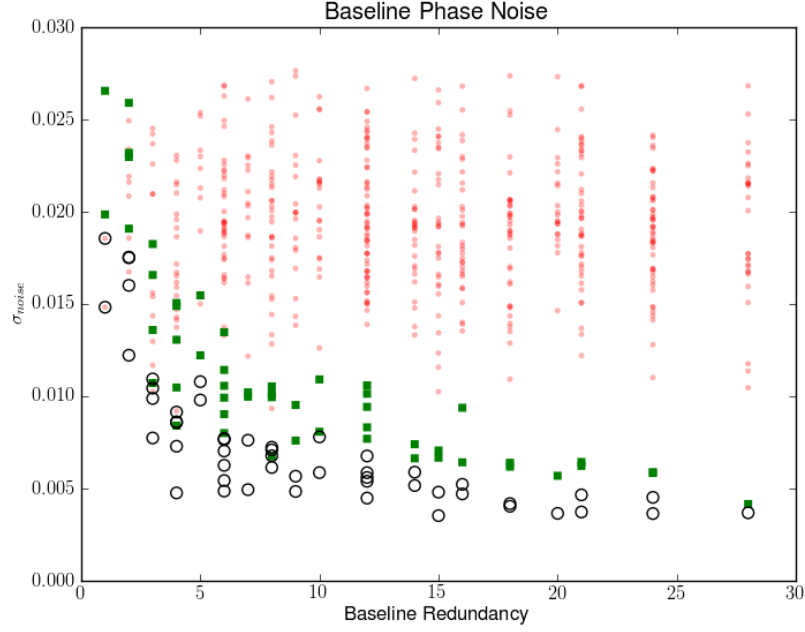
Figure 18. Phase noise for each baseline during observation plotted against the the number of redundant baselines. Red dots are for the FX correlator. Black circles are the phase noise after averaging together a set of redundant baselines. This expectedly decreases as $\frac{1}{\sqrt{n}}$ on the more redundant spacings. Green squares are the spatial FFT baselines, which are effectively an average of all the redundant spacing baselines. The spatial FFT baseline noise also decreased at a rate similar to the averaged FX correlator baselines. Though the spatial FFT phase noise is $.48 \pm .26$ higher than the FX averaged baselines in this data set.